Structural analysis of the dynamic response of a shape memory alloy based damper

Frédéric Thiebaud, Tarak Ben Zineb

To cite this version:

Frédéric Thiebaud, Tarak Ben Zineb. Structural analysis of the dynamic response of a shape memory alloy based damper. Journal of Vibration and Control, 2024, ⟨10.1177/10775463241263374⟩. ⟨hal-04732046⟩

HAL Id: hal-04732046
https://hal.science/hal-04732046v1

Submitted on 21 Oct 2024

Proof Central

Dear Author

Please use this PDF proof to check the layout of your article. If you would like any changes to be made to the layout, you can leave instructions in the online proofing interface. First, return to the online proofing interface by clicking "Edit" at the top page, then insert a Comment in the relevant location. Making your changes directly in the online proofing interface is the quickest, easiest way to correct and submit your proof.

Please note that changes made to the article in the online proofing interface will be added to the article before publication, but are not reflected in this PDF proof.

If you would prefer to submit your corrections by annotating the PDF proof,
please download and submit an annotatable PDF proof by clicking the link below.

Annotate PDF

Page Proof Instructions and Queries

Journal Title: Journal of Vibration and Control (JVC)

Article Number: 1263374

Thank you for choosing to publish with us. This is your final opportunity to ensure your article will be accurate at publication. Please review your proof carefully and respond to the queries using the circled tools in the image below, which are available **by clicking “Comment”** from the right-side menu in Adobe Reader DC.*

Please use *only* the tools circled in the image, as edits via other tools/methods can be lost during file conversion. For comments, questions, or formatting requests, please use T. Please do *not* use comment bubbles/sticky notes 💬.

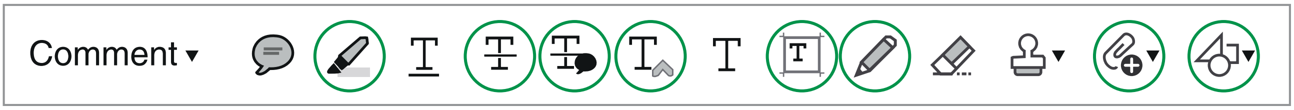

*If you do not see these tools, please ensure you have opened this file with Adobe Reader DC, available for free at get.adobe.com/reader or by going to Help > Check for Updates within other versions of Reader. For more detailed instructions, please see us.sagepub.com/ReaderXProofs.

No.	Query
	Please note that we cannot add/amend ORCID iDs for any article at the proof stage. Following ORCID’s guidelines, the publisher can include only ORCID iDs that the authors have specifically validated for each manuscript prior to official acceptance for publication.
	Please confirm that all author information, including names, affiliations, sequence, and contact details, is correct.
	Please review the entire document for typographical errors, mathematical errors, and any other necessary corrections; check headings, tables, and figures.
	Please confirm that the Funding and Conflict of Interest statements are accurate.
	Please ensure that you have obtained and enclosed all necessary permissions for the reproduction of artistic works, (e.g. illustrations, photographs, charts, maps, other visual material, etc.) not owned by yourself. Please refer to your publishing agreement for further information.
	Please note that this proof represents your final opportunity to review your article prior to publication, so please do send all of your changes now.
AQ: 0	There are no queries in this article.

Special Issue: ECCOMAS SMART 2023

Journal of Vibration and Control
2024, Vol. 0(0) 1–12
© The Author(s) 2024
Article reuse guidelines:
sagepub.com/journals-permissions
DOI: 10.1177/10775463241263374
journals.sagepub.com/home/jvc
Sage

Structural analysis of the dynamic response of a shape memory alloy based damper

Frédéric Thiebaud and Tarak Ben Zineb

Abstract

Shape memory alloys (SMAs) are promising candidates for use in sensors, actuators, or passive dampers. This paper investigates the dynamic response of a superelastic NiTi holed disk to assess its damping performance relative to frequency and temperature for SMA-based damper applications. This study involved several key steps. Initially, the superelastic behavior of the SMA was experimentally characterized through tensile tests. This testing campaign provided the required data to identify material parameters of a thermomechanical constitutive model, already implemented in the finite element code Abaqus. Using the identified parameters, a finite element based structural analysis was conducted to predict the disk's operational range, ensuring it remained within the superelastic domain without incurring potential damage. Following this static analysis, a dynamic mechanical analysis (DMA) was performed on the disk. By employing a complex stiffness approach, we further examined the disk's damping effects. This dynamic method enabled a detailed description of the apparent stiffness and damping characteristics based on solicitation frequency, test temperature, vibration amplitude, and a pre-defined static displacement. The results indicated a clearly predominant structural effect over the phase transformation effect, despite the disk's substantial damping potential.

Keywords

shape memory alloys, superelastic behavior, damping effect, dynamic mechanical analysis, equivalent complex stiffness

1. Introduction

Shape memory alloys (SMAs) are extensively studied for their potential applications in smart systems such as dampers, absorbers and actuator elements. For damping applications, a comprehensive understanding of the material's dynamic behavior is essential. The damping properties of SMAs arise from the energy dissipation associated with the martensitic transformation between the mother phase, austenite (A) and the product phase, martensite (M). This transformation's dissipative nature in SMA based dampers enables energy absorption for seismic applications as demonstrated in studies by Bono and Tirelli (1999), Tirelli et al. (2000), Dolce et al. (2001), Piedboeuf et al. (1998), and Fang et al. (2016). Recent research on passive damping and vibration control notably by Dabhi and Jani (2023), Gur et al. (2022), Zhang et al. (2020), and Lu et al. (2022) further underscores this potential. A comprehensive review on this vast topic was provided several years ago by Janke et al. (2005) and has been updated by Kalita et al. (2024).

This growing interest has spurred numerous studies on modeling the dynamic behavior and damping effects of SMAs, including contributions from Gandhi and Wolons (1999), Collet et al. (2001), Amarante Dos Santos and Cismasiu (2010), and Kong et al. (2024). The superelastic effect of Iron-Based SMAs for damping applications was also recently investigated by Megdiche et al. (2020). To conclude, a notable review by Tabrizikahou et al. (2022) discusses SMA applications and modeling for structural vibration control.

The current state of the art reveals a predominant focus on modeling the damping effect. A study on dampers designed from superelastic SMAs hence presents itself as an original approach given the little amount of work that has followed this direction. Similar approaches have been explored by Fang et al. (2016) on Belleville washers, Mirzaeifar et al. (2011) on helical springs, Barati et al. (2022) on an annular circular plate, and Danesh et al. (2023) on a clamped beam. This paper aims to contribute to this research direction.

CNRS, Arts et Métiers ParisTech, Université de Lorraine, Nancy, France

Received: 30 October 2023; revised: 31 May 2024; accepted: 4 June 2024

Corresponding author:
Frédéric Thiebaud, Université de Lorraine, CNRS, Arts et Métiers ParisTech, LEM3, F-54000, Nancy, France.
Email: frederic.thiebaud@univ-lorraine.fr

It presents the dynamical characterization and evaluation of the damping effect of an innovative superelastic damper designed as a holed disk etched from a NiTi superelastic plate.

The first part, details the damper's geometrical characteristics and the identification of the SMAs' thermomechanical behavior under quasi-static loading, achieved through tensile tests at room temperature and at a quasi-static rate. The second part involves developing a finite element based numerical tool focused on the holed disk to predict the range of the amplitude of vibrations that activates the superelastic mode, thereby inducing a damping effect. This tool utilizes a constitutive model of the SMA's thermomechanical behavior developed by Chemisky et al. (2011) and implemented in Abaqus© via a UMAT subroutine necessitating the identification of the superelastic parameters of the NiTi SMA. Numerical simulations of cyclic tensile tests of the damper allowed to identify the amplitude range for its effective use. The third part includes a dynamic mechanical analysis (DMA) to evaluate the structure's damping effect as a function of various parameters such as the vibration amplitude (in the considered range), frequency and static pre-displacement, at three temperatures (cold (10°C), warm (40°C), and room temperature (21°C)). The damping effect is modeled using the innovative concept of the equivalent complex stiffness previously presented by Thiebaud and Ben Zineb (2014) and recalled in this paper.

The results clearly demonstrate the existence of an optimized set of parameters enhances the structure's damping effect.

Therefore, this article is structured as follows:

1. Static characterization of the SMA behavior and the damper's response
   (a) Design of the damper
   (b) Superelastic behavior of the NiTi SMA
   (c) SMA's Thermodynamic behavior modeling
   (d) Identification of the material parameters
   (e) Numerical simulations
2. Dynamical behavior of the damper
   (a) Equivalent complex stiffness
   (b) Influence of the frequency and the amplitude
   (c) Influence of a predisplacement and the amplitude
3. Conclusion

2. Static characterization of the SMA's behavior and the damper's response

2.1. Design of the damper

The design of the studied damper draws inspiration from the spring shapes used in classical shakers. This spring features numerous symmetrically arranged oblong holes, revealing small beams that will work in bending. This unique geometry makes it an interesting subject for studying single-degree-of-freedom damping structures, adding to the existing body of research in this field.

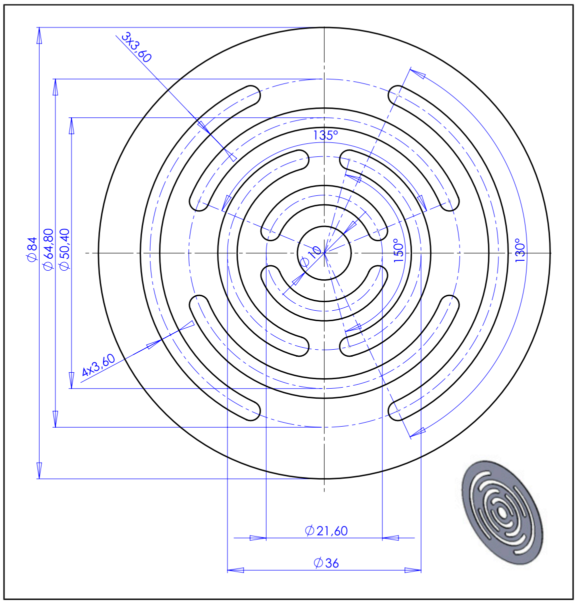

Figure 1. Geometry of the damper and its dimension. Its thickness is about 0.6 mm.

Our damper presents itself as a disk with a main diameter of 84 mm, machined by wire-cut electric discharge process from a main NiTi superelastic plate provided by Nimesis© (France). The plate has a thickness of approximately 0.6 mm. The geometry and dimensions of the disk are specified in Figure 1.

2.2. Superelastic behavior of the NiTi SMA

There are numerous macroscopic behavior models for SMAs that facilitate structural design, many of which incorporate specific SMA characteristics such as tension-compression asymmetry and thermo-mechanical coupling. Notable examples include the models developed by Auricchio and Taylor (1997), Popov and Lagoudas (2007), Leclercq and Lexcellent (1996), Saint-Sulpice et al. (2009), and Xu et al. (2021). A comprehensive synthesis of these models is presented by Cisse et al. (2016).

To activate the superelastic behavior of the SMA, an initial heat treatment is required. This treatment involves heating the material to 300°C for 15 min followed by a water quenching. Tensile samples, each 3 mm wide, are then cut from the main plate in a standard shape for tensile testing. Both a destructive tensile test and a cyclic test to identify the superelastic full-loop are performed. These tests help determine various thermo-mechanical parameters, such as the characteristic transformation stresses and the ultimate stress. Both tests are carried out at room temperature (21°C) with a quasi-static loading rate ($10^{-4}\cdot s^{-1}$). A

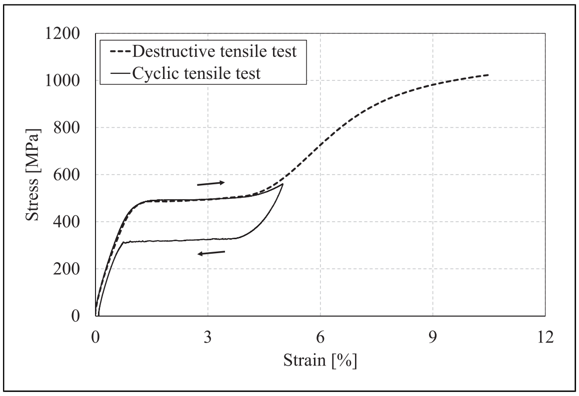

Figure 2. Destructive and cyclic tensile tests on NiTi SMA in quasi-static conditions (rate = 10^{-4}/s) and room temperature (21°C).

Zwick/Roell© tensile machine with a capacity of 100 kN is used and the strain is measured locally with a clip-on extensometer. The ASTM F2516 standard is followed for these tests. Figure 2 shows the response of the NiTi SMA for both destructive and cyclic tests. The forward transformation starts at a stress σ_{AM}^{s} = 475 MPa and finishes at σ_{AM}^{f} = 550 MPa. The reverse transformation starts at a stress σ_{MA}^{s} = 325 MPa and finishes at σ_{MA}^{f} = 310 MPa. The ultimate stress is around 1000 MPa. To prevent failure, it is preferable to maintain stress values within the range of 0 to 550 MPa, where the martensitic transformation is not yet complete.

2.3. SMA thermomechanical behavior modeling

The use of NiTi SMA is advantageous due to its hysteretic superelastic behavior, which induces a damping effect. Under these considerations, we can design a one-translational-degree-of-freedom damper. It is crucial to estimate the critical displacement applied to the damper that initiates the forward martensitic transformation at some point within the disk. Similarly, it is necessary to estimate the maximum admissible displacement applied to the damper to prevent disk failure. Typically, it is desirable for the local stress to remain below σ_{AM}^{f} thereby avoiding complete martensitic transformation. These two critical displacements are identified through static numerical simulations using a three-dimensional phenomenological constitutive model developed by Peultier et al. (2006) and enhanced by Chemisky et al. (2011). The model describes the effects of both forward and reverse martensitic transformation for SMAs. In a stress-free state, the SMA is assumed to be fully austenitic. Under thermomechanical loading, the phase can locally transform into martensite.

Considering the transformation, the twinning-induced strains and the elastic and thermal expansion strains under the assumption of small perturbations, the total strain $\underline{\varepsilon}$ is decomposed as follows

$$\underline{\varepsilon} = \underline{\varepsilon}^{e} + \underline{\varepsilon}^{th} + \underline{\varepsilon}^{t} + \underline{\varepsilon}^{twin} \tag{1}$$

where $\underline{\varepsilon}^{e}$, $\underline{\varepsilon}^{th}$, $\underline{\varepsilon}^{t}$, and $\underline{\varepsilon}^{twin}$ are, respectively, the elastic, thermal expansion, martensitic transformation, and twinning strains.

The transformation strain is determined by averaging the local transformation strain field on the Representative Volume Element (RVE). It can then be expressed as a function of the volume fraction of martensite f and the mean transformation strain $\underline{\bar{\varepsilon}}^{t}$ as depicted in equation (2)

$$f\underline{\bar{\varepsilon}}^{t} = \frac{V_M}{V}\frac{1}{V_M}\int_{V_M}\underline{\varepsilon}(r)dV \tag{2}$$

where V_M is the volume of martensite and V the total volume of the RVE. Following the same rationale, the detwinning strain is determined by averaging the local mean twins accommodation strain field on the RVE. It can then be expressed as a function of the self-accommodated martensitic volume fraction f^{FA}, the self-accommodated martensite volume V_M^{FA} and the mean twins accommodation strain $\underline{\varepsilon}^{twin}$ (equation (3))

$$f^{FA}\underline{\bar{\varepsilon}}^{twin} = \frac{V_M^{FA}}{V}\frac{1}{V_M^{FA}}\int_{V_M}\underline{\varepsilon}^{twin}(r)dV \tag{3}$$

Introducing the equations (2) and (3) and the relation between stress and elastic strain, in equation (1) yields a new expression of the total strain (equation (4))

$$\underline{\varepsilon} = \underline{\underline{S}} : \underline{\sigma} + \underline{\alpha}\left(T - T_{ref}\right) + f\underline{\bar{\varepsilon}}^{t} + f^{FA}\underline{\bar{\varepsilon}}^{twin} \tag{4}$$

where $\underline{\underline{S}}$, $\underline{\sigma}$, $\underline{\alpha}$, T, and T_{ref} are, respectively, the isotropic fourth-order compliance tensor, the effective stress tensor over the RVE, the isotropic thermal expansion tensor, the current and the reference temperatures. The first thermodynamic principle combined with the previous strain decomposition leads to the following expression of the Gibbs free energy G (equation (5))

$$\begin{aligned} G = {} & U^{A} - TS^{A} + B(T - T_0)f - \frac{1}{2}\underline{\sigma} : \underline{\underline{S}} : \underline{\sigma} \\ & - \underline{\sigma} : \underline{\alpha}(T - T_0) - \underline{\sigma} : \underline{\bar{\varepsilon}}^{T} f - \underline{\sigma} : \underline{\bar{\varepsilon}}^{twin} f^{FA} \\ & + \frac{1}{2}H_f f^{2} + \frac{1}{2} f H_{\varepsilon}\underline{\bar{\varepsilon}}^{T} : \underline{\bar{\varepsilon}}^{T} \\ & + \frac{1}{2} f^{FA} H_{twin}\underline{\bar{\varepsilon}}^{twin} : \underline{\bar{\varepsilon}}^{twin} \\ & + C_V\left[(T - T_0) - T\log\frac{T}{T_0}\right] \end{aligned} \tag{5}$$

This Gibbs free energy includes various contributions of austenite and martensite free energies and interactions between martensite variants and between grains energies. U_A, S_A, B, T_0, H_f, H_e, H_{twin}, and C_V are, respectively, the internal energy, the entropy of the austenitic phase, the difference between entropies of austenite and martensite

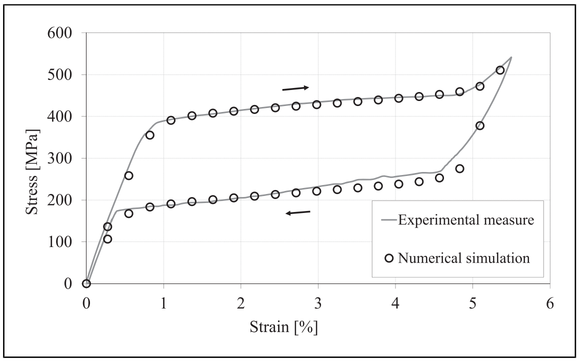

Figure 3. Comparison between the experimental and the numerical responses of the NiTi SMA after the identification of the material parameters.

which is related to the stress-temperature slope of transformation limits, the thermodynamical equilibrium temperature between austenite and martensite phases, the pseudo-hardening coefficient of phase transformation, the two material parameters describing interactions, and the latent heat coefficient.The application of the second principle of thermodynamics leads to the following expression of the Clausius–Duhem inequality depending on the Gibbs free energy G expression defined by equation (6)

$$-\frac{\partial G}{\partial \underline{\sigma}}:\dot{\underline{\sigma}}-\frac{\partial G}{\partial T}:\dot{T}-\frac{\partial G}{\partial V_k}:\dot{V}_k-\dot{\underline{\sigma}}:\underline{\varepsilon}-\vec{q}\cdot\frac{\overrightarrow{\text{grad}T}}{T}\geqslant 0 \quad (6)$$

In this equation, the Gibbs free energy is expressed as a function of state variables, $(\underline{\sigma}, T)$, internal variables $\left(V_k = f, f^{FA}, \underline{\bar{\varepsilon}}^T, \underline{\bar{\varepsilon}}^{twin}\right)$ and material constants. From this expression, one can derive the driving forces related to state and internal variables, as detailed by Chemisky et al. (2011). To describe the hysteretic property of martensitic phase transformation and reorientation, yield forces are assigned to each of the three driving forces associated with phase transformation, orientation, and twins accommodation criteria, which together allow to form the phase transformation diagram. Based on these criteria and their rates, the activation of mechanisms (the transformation, orientation, and accommodation of twins) and evolution laws of internal variables are deduced by assuming the consistency condition. A specific evolution law is adopted for f^{FA} depending on f

$$\dot{f}^{FA}=\xi^{FA}\dot{f}\begin{cases}\xi^{FA}=\dfrac{\varepsilon^T_{SAT}-\bar{\varepsilon}^T_{eq}}{\varepsilon^T_{SAT}}, \text{if}\,\dot{f}>0\\[2ex] \xi^{FA}=\dfrac{f_r^{FA}}{f_r}, \text{if}\,\dot{f}<0\end{cases} \quad (7)$$

where ε^T_{SAT}, $\bar{\varepsilon}^T_{eq}$, f_r, and f_r^{FA} are, respectively, a material parameter characterizing the maximum transformation strain, the von Mises equivalent mean transformation strain, the martensite and the self-accommodated volume fractions during reverse transformation. This model takes nonsymmetric behavior between tension and compression into account by making the maximum mean transformation strain dependent on the second and third stress invariants.

To perform structural analysis of SMAs applications using the finite element method, this behavior model is implemented in the Abaqus© FEM code via the user subroutine UMAT. The non-linear problem is then solved by using an implicit, iterative Newton–Raphson numerical scheme.

2.4. *Identification of the material parameters*

Many parameters are necessary to accurately describe this phenomenological constitutive model. To identify these parameters, multiple numerical cyclic tensile tests are performed to fit the cyclic experimental curve shown in Figure 2. The results of the final simulation with the identified NiTi material parameters, presented in Figure 3 demonstrate a consistent correlation between both experimental and numerical results. The adjusted NiTi material parameters required for the phenomenological model are provided in Table 1. Note that the transformation temperature was supplied by the provider and directly used in these numerical simulations.

2.5. *Numerical simulation*

Due to the symmetric conditions, only a quarter of the damper is modeled (Figure 4). The holed disk is discretized using a random meshing technique resulting in 247 S4R shell elements with 756 degrees of freedom. The S4R element is a 4-nodes, quadrilateral, stress-shell element with reduced integration and a large strain formulation. The external curved edge of the disk is clamped and a normal displacement amplitude of 25 mm is applied to its internal curved edge. Symmetric conditions in the $\vec{x}$ and $\vec{y}$ directions (Xsymm and Ysymm, respectively) are imposed on the corresponding straight edges. The axial reaction force is measured on a reference point connected to the internal curved edge. The automatic time increment option in Abaqus© is used with an initial estimate of dividing the loading and unloading steps into 1000 increments, and the geometrical non-linearity option is activated. The non-linear numerical problem is solved by using an implicit, iterative Newton–Raphson numerical scheme.

In addition to this numerical predictive simulation, a corresponding experimental cyclic test was performed on the Zwick/Roell© tensile machine at room temperature (21°C) with a quasi-static loading rate ($10^{-4}\cdot s^{-1}$). Figure 5 shows the evolution of the reaction force of the damper versus the imposed displacement obtained from both the numerical simulation and the experimental test. Overall, the numerical curve follows the same trend as the experimental

Table 1. Identified NiTi material parameters.

Parameter	Description	Columns
E	Young's modulus	50 GPa
ν	Poisson's coefficient	0.3
α	Dilatation coefficient	0
$\varepsilon^{tr}_{\max}$	max. tension strain	0.035
R_f	Internal loops amplitude	0.6
$F^{\max}_{\varepsilon^T}$	Reorientation yield stress	120
H_f	Transformation interaction	1 MPa
H_{eps}	Hardening reorientation	2500 MPa
H_{twin}	Hardening twins accommodation	40000 MPa
ε^{c}_{max}	max. compression strain	0.035
$b^T_{M_s}$	Direct transformation slope	5 MPa/°C
$b^T_{A_f}$	Reverse transformation slope	5 MPa/°C
M_s	A → M start transformation temp.	−75
A_f	A → M finish transformation temp.	−30
H_s	Martensite stabilization coefficient	10

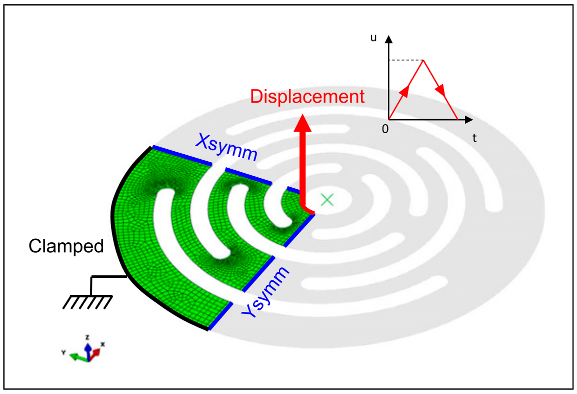

Figure 4. Finite element model of the SMA holed plate.

one displaying a nonlinear response with hysteretic behavior. However, some quantitative differences persist, ranging from 9.5 to 10%. These quantitative differences can be attributed to the modeling of a fixed connection between the outer edge of the disk and the grip. Despite this, the level of accuracy can be considered sufficient for a predictive approach, allowing determination of the operating range of the disk and examination of local quantities at the oblong holes, away from the external edge. Consequently, this result successfully validates the material parameters identification procedure. Thus, the numerical model can be deemed a reliable tool for predicting the equilibrium state, stress, strain, and volume fraction of martensite distributions within the damper as a function of the imposed displacement.

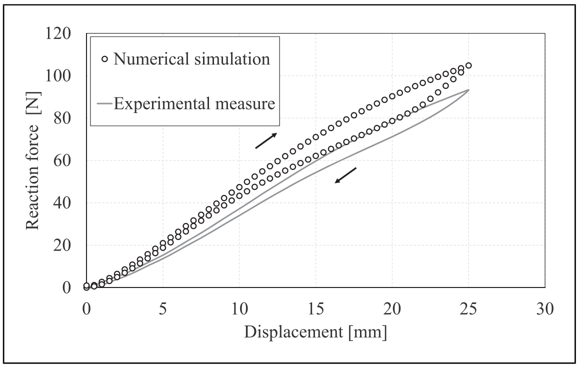

Figure 5. Comparison between the numerical and the experimental responses of the NiTi holed plate.

This numerical tool is now used to identify (i) the required imposed displacement when the forward martensite transformation $(\sigma_{VM} = \sigma^s_{AM})$ begins somewhere inside the damper and (ii) the maximum required displacement when the forward martensite transformation ends $(\sigma_{VM} = \sigma^f_{AM})$. Note that σ_{VM} is the equivalent von Mises stress.

Figure 6, shows that the forward martensitic transformation begins inside the damper for an imposed displacement of 11 mm. At this state, martensite localization occurs with the maximum von Mises stress observed at the extremities of the oblong holes. For this imposed displacement, the von Mises stress σ_{VM} is about 487 MPa and the volume fraction of martensite is approximately 40%. Both these values correspond to the middle region around the forward martensitic transformation plateau (Figure 3), where the apparent stiffness of the material is low. The right part of Figure 6 shows the displacement, von Mises stress, and volume fraction of martensite distributions for an imposed displacement of 25 mm. At this level of solicitation, the damper is highly deformed, the rotation effects are significant, which is not adapted for a damping technical use. The von Mises stress is about 552 MPa and the volume fraction of martensite is about 86%, corresponding to the end of the forward transformation. Beyond this displacement loading, fatigue effects due to cyclic solicitations significantly increase, leading to damper failure. Consequently, it is advisable not to exceed a displacement of 25 mm, with an imposed displacement of about 20 mm being a safer limit.

Furthermore, it is observed that the martensitic transformation is highly localized at the extremities of the oblong holes, where high values of the volume fraction of martensite are measured, while it diminishes quickly within the interior of the disk. This indicates that the structural effect of the disk predominates over the transformation phase. This result is confirmed in Figure 7, which shows a static cyclic tensile test of the damper at three displacement amplitudes: 15, 20, and 25 mm. The hysteresis is essentially zero at a displacement amplitude of about 15 mm, moderate at 20 mm, and more significant at 25 mm. This further indicates that the structural effect prevails over the transformation phase.

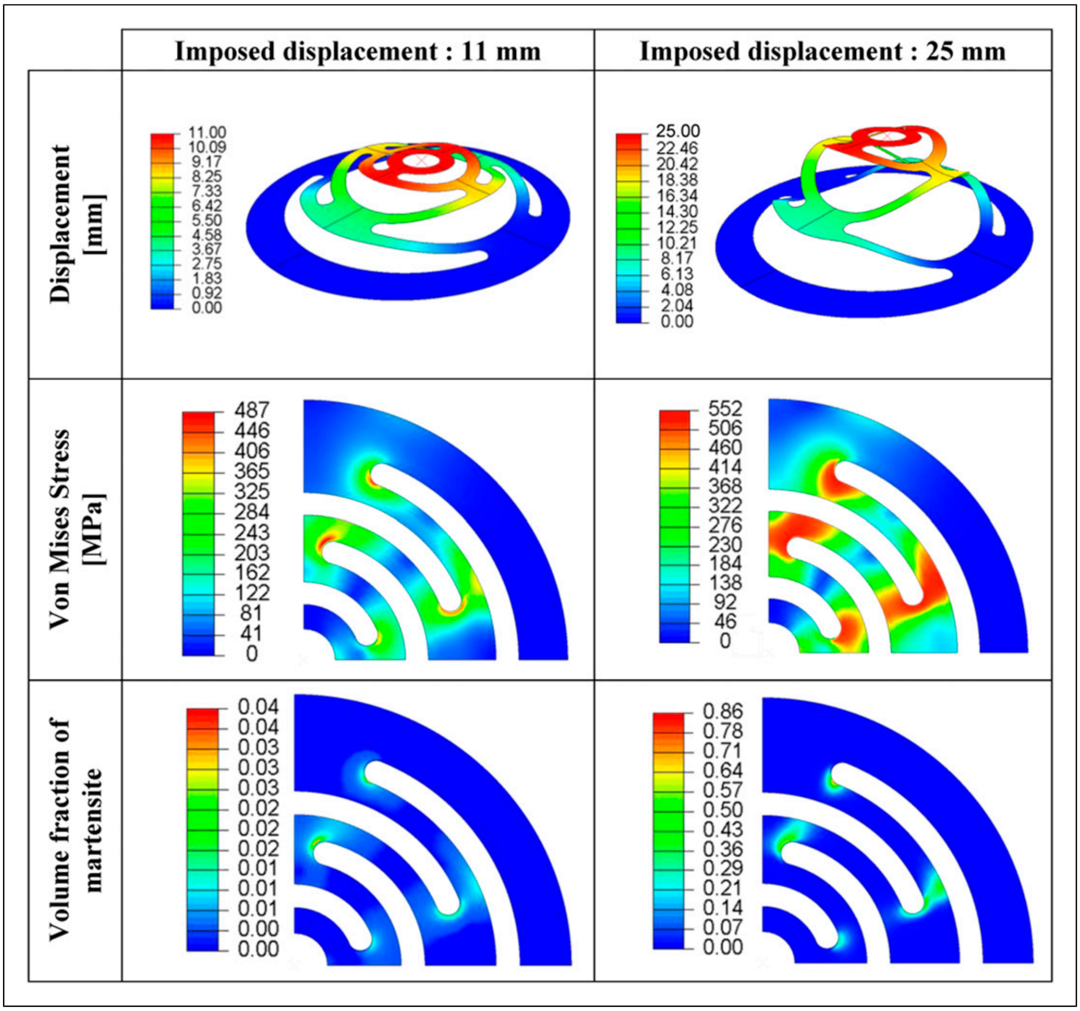

Figure 6. Displacement, Von Mises stress and volume fraction of martensite in the holed disk for an imposed displacement about 11 mm and 25 mm.

As a result of this initial numerical static simulation of the holed disk, the maximum imposed displacement for the Dynamic Mechanical Analysis (DMA) experimental tests will be limited to about 20 mm to prevent fatigue effects and avoid failure of the disk.

3. Dynamical behavior of the damper

The dynamic tensile tests are conducted using a Dynamic Mechanical Analysis (DMA) (Figure 8). The Zwick/Roell© LTM1 driven by the software TestXpert R© is utilized to measure the storage modulus and the loss factor as a function of various parameters such as amplitude, pre-displacement, and frequency at a given temperature. Additionally, experimental tests are carried out at three temperatures: a “cold” temperature (10°C), room temperature (20°C), and a “high” temperature (40°C). The tensile machine is equipped with a heat chamber and a nitrogen tank to generate the cold and warm temperatures.

The displacement is imposed by the brushless linear motor of the DMA tensile machine and the resulting force is measured by a load cell with a capacity of 1 kN. In a post-treatment process, the damping effect is investigated by calculating the storage stiffness and the loss factor. These two parameters are modeled using the equivalent complex stiffness approach which is detailed in the following section.

3.1. Equivalent complex stiffness

In order to characterize the damping effect of the structure, the equivalent complex stiffness model based on the Valanis endochronic theory Valanis (1970) is presented in this section.

Firstly, consider a vibrating displacement solicitation u of the damper at the pulsation ω and an amplitude u_m

$$u(u_m, \omega) = u_m \, sin(\omega t) \tag{8}$$

The reaction force F can be decomposed into a Fourier series as follows

$$F(t) = F_0(\omega) + \sum_{n=1}^{+\infty} a_n(\omega)\cos(n\omega t) + b_n(\omega)\sin(n\omega t) \tag{9}$$

where a_n and b_n are the classical Fourier coefficients and F_0 the static component of F. By considering the harmonic balance approximation, we can rewrite F focusing on its first harmonic as

$$F(t) \simeq A(\omega)\sin(\omega t + \phi(\omega)) \tag{10}$$

where A and Φ are, respectively, the amplitude and the phase of F. The previous expression leads to the complex expression $\tilde{F}$ of the resulting force F

$$\tilde{F}(u_m, \omega) = A(u_m, \omega) e^{(i\omega t + \Phi(u_m, \omega))} \tag{11}$$

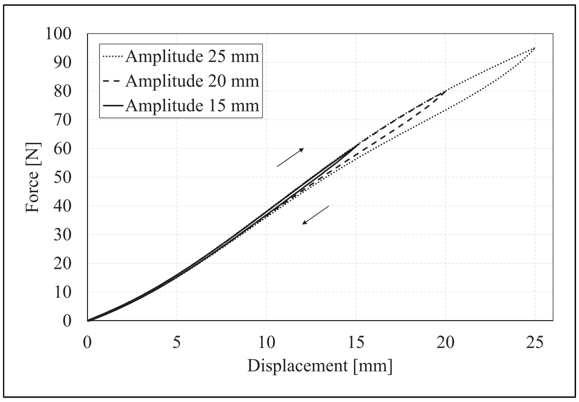

Figure 7. Numerical static cyclic tests of the damper at room temperature.

where

$$A(u_m, \omega) = \left[\left(\frac{\omega}{\pi u_m} \int_0^T F(t)\cos(\omega t) dt \right)^2 \right. \tag{12}$$

$$\left. + \left(\frac{\omega}{\pi u_m} \int_0^T F(t)\sin(\omega t) dt \right)^2 \right]^{\frac{1}{2}} \tag{13}$$

and

$$\Phi(u_m, \omega = Arctan \left(\frac{\int_0^T F(t)cos(\omega t)dt}{\int_0^T F(t)sin(\omega t)dt} \right) \tag{14}$$

The dynamic stiffness $\tilde{K}$ is also defined as the ratio between the complex reaction force $\tilde{F}$ and the complex imposed displacement $\tilde{u}$

$$\tilde{K}(u_m, \omega) = \frac{\tilde{F}(u_m, \omega)}{\tilde{u}(u_m, \omega)} \tag{15}$$

where the complex expression of the imposed displacement $\tilde{u}$ is defined as

$$\tilde{u} = u_m e^{i\omega t} \tag{16}$$

We can now derive the explicit expression of the equivalent stiffness

$$\tilde{K}(u_m, \omega) = K(u_m, \omega)(1 + i\eta(u_m, \omega)) \tag{17}$$

where K is the storage stiffness and η the loss factor. These expressions are, respectively

$$K(u_m, \omega) \quad = \quad \frac{\omega}{\pi u_m} \int_0^T F(t)cos(\omega t)dt \tag{18}$$

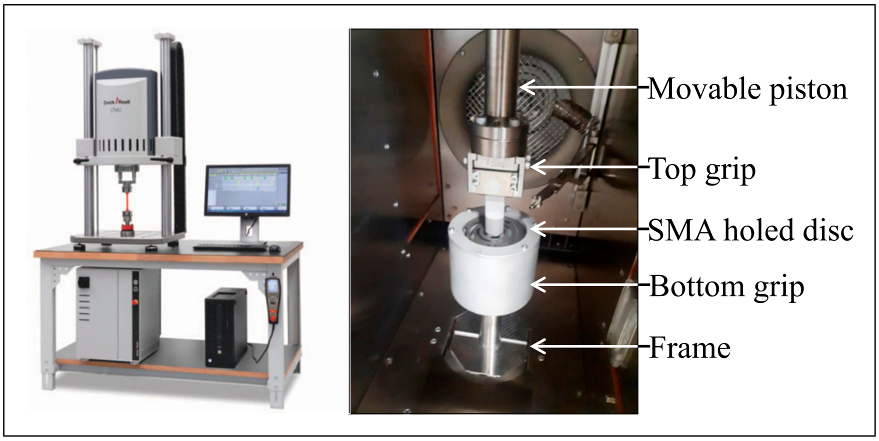

Figure 8. Zwick/Roell© LTM1 Dynamic Mechanical Analysis (DMA) tensile machine and detail of the experimental device with the thermal chamber.

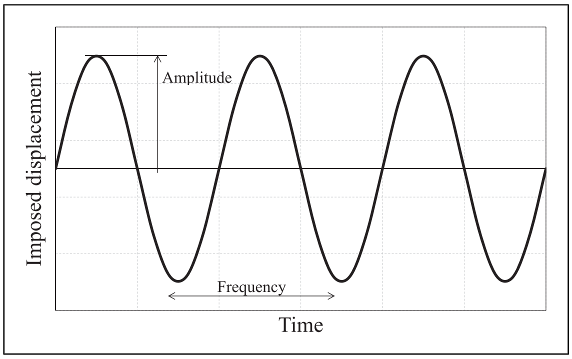

Figure 9. First mechanical solicitation of the damper: symmetric imposed displacement to the damper for the first DMA test.

$$\eta(u_m,\omega) = \frac{\int_0^T F(t)cos(\omega t)dt}{\int_0^T F(t)sin(\omega t)dt} \tag{19}$$

These two parameters, K and η are directly calculated by the software TestXpert R© after each test.

3.2. Influence of the frequency and the amplitude

In this section, the dynamic response of the damper is analyzed as a function of the amplitude of symmetric vibrations (Figure 9) in the range [4–20 mm] at three

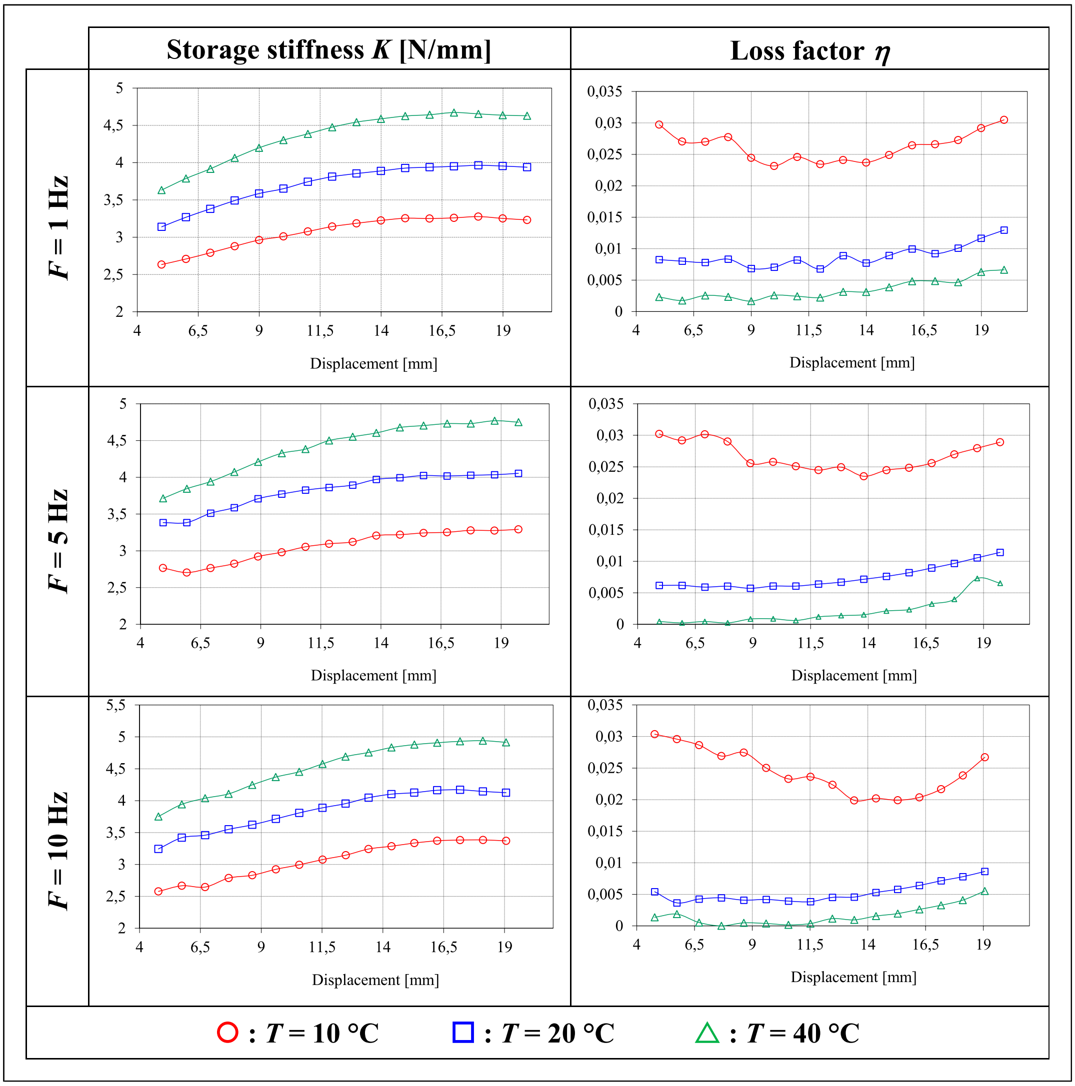

Figure 10. Evolution of the dynamic stiffness and the loss factor versus the amplitude of displacement at three temperatures, for a given frequency.

frequencies: 1, 5, and 10 Hz (Figure 9) and at three temperatures: 10, 20, and 40°C.

Figure 10 illustrates the evolution of the dynamic stiffness and the loss factor versus the amplitude of displacement at three temperatures (color lines: red for 10°C, blue for 20°C, and green for 40°C), and for three frequencies (1 Hz, 5 Hz, and 10 Hz on each line of the table). Similarly, Figure 11 presents the evolution of the same parameters: dynamic stiffness and loss factor versus the amplitude of displacement at three frequencies (color lines: red for 1 Hz, blue for 5 Hz, and green for 10 Hz) and for three temperatures (10°C, 20°C, and 40°C on each line of the table).

For a given frequency (Figure 10), and for each temperature, an increase in dynamic stiffness is observed in the range [4–14 mm] followed by a stabilization at displacement amplitudes higher than 14 mm. This result is corroborated by the study of the loss factor: an increase in this parameter is noted for vibration amplitudes exceeding 14 mm, for a given frequency and for each temperature. This phenomenon can be explained by the fact that for vibration amplitudes below 14 mm, the martensitic transformation is insufficient to induce a significant damping effect on the structure. However, the optimal damping effect for this damper is observed only in the range [10–14 mm], which is a major limitation for its performance. Beyond this range, fatigue effects and subsequent fracture phenomena will occur within the disk. Furthermore, for a given amplitude displacement, an increase (and thus a decrease) in dynamic stiffness (the loss factor) is observed with rising temperatures. This indicates that the damper performs better in colder conditions. Specifically, the loss factor measured at 10°C is three times higher than those measured at 20 and 40°C. Lastly, the influence of the frequency is not significant: the dynamic stiffness values represented in Figure 11 are very similar. This can be further explained by the fact that, for vibrating

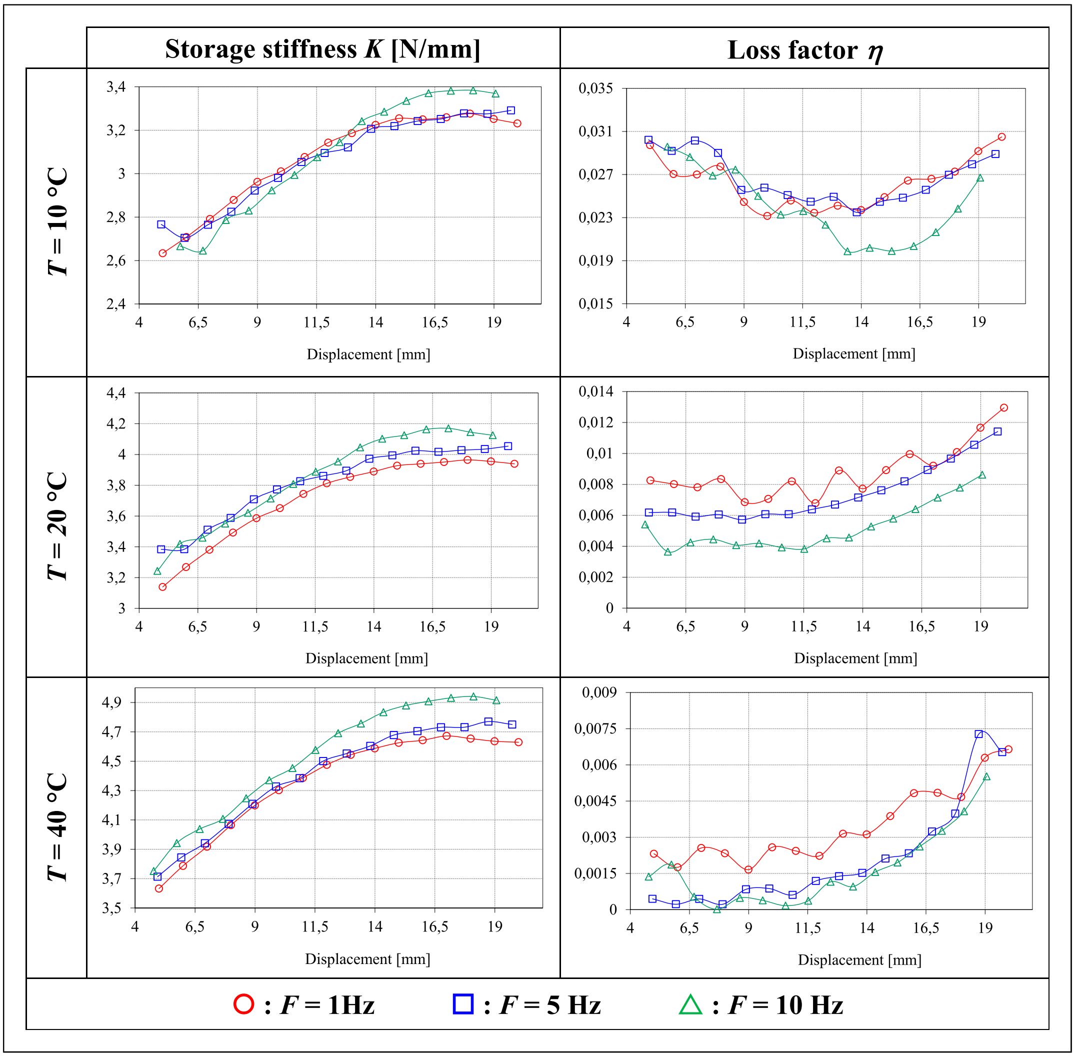

Figure 11. Evolution of the dynamic stiffness and the loss factor versus the amplitude of displacement at three frequencies, for a given temperature.

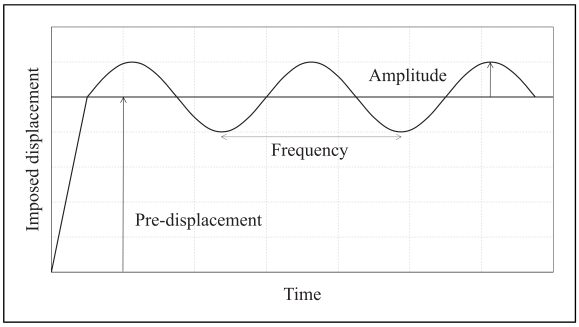

Figure 12. Second mechanical solicitation of the damper: vibrations displacement state around a static displacement offset.

solicitations, the stable adiabatic behavior of the SMA is quickly achieved, resulting in no significant variations in the expression of the storage stiffness and loss factor. Consequently, for this type of solicitation, the best performance of the damper is achieved at low temperatures and high vibration amplitudes, regardless of the imposed frequencies.

3.3. *Influence of a predisplacement and the amplitude*

In this section, the dynamic response of the damper is analyzed as a function of static pre-displacement and vibration amplitude. The static strain offset is achieved linearly as shown in Figure 12.

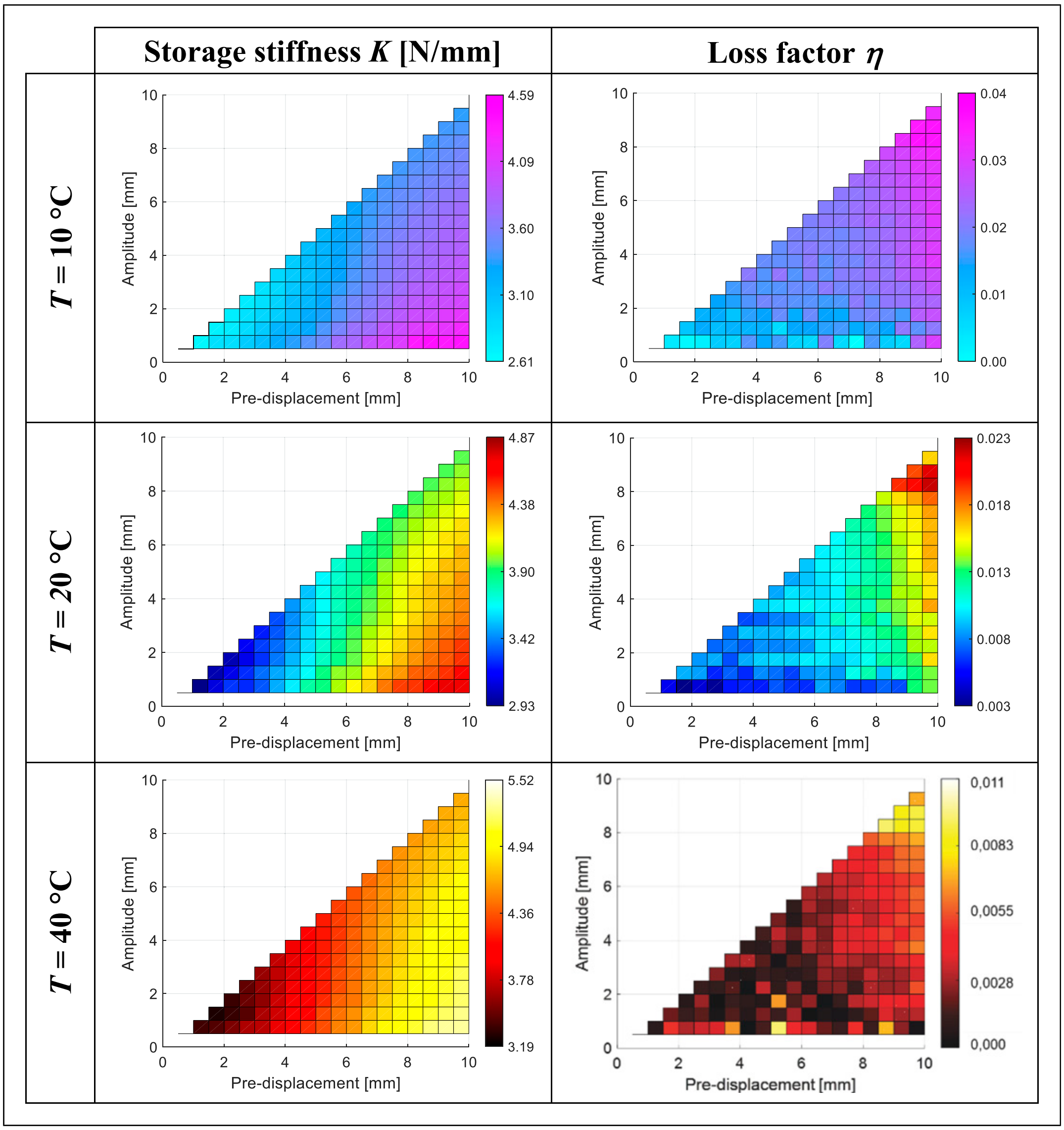

Figure 13. Evolution of the dynamic stiffness and the loss factor versus the pre-displacement and the displacement for three temperatures.

Technologically, the static offset corresponds to an imposed offset, while vibration amplitude represents an external unknown solicitation. For these tests, the frequency is set to 1 Hz. The range of the imposed pre-displacement is [0.5–10 mm], and the maximum vibration amplitude for a given pre-displacement is equal to half of said pre-displacement.

Figure 13 shows the evolution of the dynamic stiffness and the loss factor versus the imposed pre-displacement and the vibration amplitude for three temperatures: 10, 20, and 40°C. The study of the loss factor clearly indicates that for each temperature, the best damping performance is achieved at the maximum static offset and maximum vibration amplitude. Under these conditions, the static offset corresponds to the beginning of the forward martensitic transformation, hence a significant loss of the structure's stiffness. Similarly, the maximum vibration amplitude results in maximum hysteresis and, consequently, maximum dissipation. Under these optimal conditions, an increase of the dynamic stiffness with increasing temperature is observed. This result is consistent with findings previously shown in Figure 11.

4. Conclusion

In this paper, the experimental dynamic mechanical analysis (DMA) of an innovating NiTi holed disk is presented. This investigation led to the characterization of the damping effect using the equivalent complex stiffness method. Initially, a numerical tool employing a phenomenological constitutive model for the SMA superelastic effect was implemented in Abaqus© via a UMAT user subroutine. This numerical tool enabled the determination of the minimum vibration amplitude at which martensitic transformation begins inside the disk as well as the maximum vibration amplitude allowed to prevent damage effects within the disk. Within this range of vibration amplitudes, various parameters such as frequency, vibration amplitude, and static pre-displacement offset were analyzed at three temperatures: a cold temperature (10°C), room temperature (20°C), and a warm temperature (40°C). The results clearly demonstrate the existence of a specific set of parameters that optimize the damping effect of the disk. This work opens up several future research prospects that we aim to further explore. For instance, the influence of different SMA materials (NiTi-Nb, CuAlBe, CuZnAl, …) and optimizing the disk design to prevent stress concentration at the oblong holes extremities. Finally, the generated experimental database will facilitate the development of a numerical tool aimed at optimizing and implementing control applications in civil engineering using the same methodology.

Declaration of conflicting interests

The author(s) declared no potential conflicts of interest with respect to the research, authorship, and/or publication of this article.

Funding

The author(s) received no financial support for the research, authorship, and/or publication of this article.

ORCID iD

Frédéric Thiebaud https://orcid.org/0000-0001-8229-672X

References

Amarante Dos Santos F and Cismasiu C (2010) Comparison between two sma constitutive models for seismic applications. *Journal of Vibration and Control* 16(6): 897–914.

Auricchio F and Taylor RL (1997) Shape-memory alloys: modelling and numerical simulations of the finite-strain superelastic behavior. *Computer Methods in Applied Mechanics and Engineering* 143(1-2): 175–194.

Barati AHN, Jafari AA, Haghighi SE, et al. (2022) Dynamic response of an annular circular plate made of shape memory alloy using differential quadrature method. *Proceedings of the Institution of Mechanical Engineers - Part C: Journal of Mechanical Engineering Science* 236(11): 5836–5849.

Bono F and Tirelli D (1999) *Characterisation of materials for the innovative antiseismic techniques*. JRC ISPRA, Internal Report.

Chemisky Y, Duval A, Patoor E, et al. (2011) Constitutive model for shape memory alloys including phase transformation, martensitic reorientation and twins accommodation. *Mechanics of Materials* 43(7): 361–376.

Cisse C, Zaki W and Ben Zineb T (2016) A review of constitutive models and modeling techniques for shape memory alloys. *International Journal of Plasticity* 76: 244–284.

Collet M, Foltête E and Lexcellent C (2001) Analysis of the behavior of a shape memory alloy beam under dynamical loading. *European Journal of Mechanics - A: Solids* 20(4): 615–630.

Dabhi O and Jani Y (2023) Seismic response control of parallel structures connected by passive shape memory alloy damper. In: AIP Conference Proceedings, Vol. 2963. AIP Publishing.

Danesh N, Mahmoodabadi M and Fathi A (2023) Investigation of the damping performance of a shape memory alloy beam. *International Journal of Engineering* 36(7): 1369–1382.

Dolce M, Cardone D and Marnetto R (2001) Sma recentering devices for seismic isolation of civil structures. *Smart structures and materials 2001: Smart systems for bridges, structures, and highways* 4330: 238–249.

Fang C, Zhou X, Osofero AI, et al. (2016) Superelastic sma belleville washers for seismic resisting applications: experimental study and modelling strategy. *Smart Materials and Structures* 25(10): 105013.

Gandhi F and Wolons D (1999) Characterization of the pseudoelastic damping behavior of shape memory alloy wires using complex modulus. *Smart Materials and Structures* 8(1): 49–56. DOI: 10.1088/0964-1726/8/1/005.

Gur S, Roy K and Singh P (2022) Seismic performance assessment of adjacent building structures connected with superelastic shape memory alloy damper and comparison with yield damper. *Structural Control and Health Monitoring* 29(5): e2926.

Janke L, Czaderski C, Motavalli M, et al. (2005) Applications of shape memory alloys in civil engineering structures—overview, limits and new ideas. *Materials and Structures* 38: 578–592.

Kalita U, Guntu R, Seelam R, et al. (2024) A review on the shape memory alloy, vibration dampers used in uavs. In: AIP Conference Proceedings, Vol. 2962. AIP Publishing.

Kong S, Zhao G, Ma Y, et al. (2024) A novel response-amplified shape memory alloy-based damper: theory, experiment and numerical simulation. *Soil Dynamics and Earthquake Engineering* 176: 108291.

Leclercq S and Lexcellent C (1996) A general macroscopic description of the thermomechanical behavior of shape memory alloys. *Journal of the Mechanics and Physics of Solids* 44(6): 953–980.

Lu Z, Rong K, Tian L, et al. (2022) Studies on the damping mechanism of shape memory alloy-spring tuned vibration absorber attached to a multi-degree-of-freedom structure. *Journal of Vibration and Control* 28(19-20): 2666–2677.

Megdiche M, Sallami A, Thiebaud F, et al. (2020) Experimental analysis of the pseudoelastic damping capacity of the fe-30mn-6si-5cr shape memory alloy. *Smart Materials and Structures* 29(8): 084002.

Mirzaeifar R, DesRoches R and Yavari A (2011) A combined analytical, numerical, and experimental study of shape memory alloy helical springs. *International Journal of Solids and Structures* 48(3-4): 611–624.

Peultier B, Ben Zineb T and Patoor E (2006) Macroscopic constitutive law of shape memory alloy thermomechanical behaviour. Application to structure computation by fem. *Mechanics of Materials* 38(5): 510–524, Shape Memory Alloys.

Piedboeuf M, Gauvin R and Thomas M (1998) Damping behaviour of shape memory alloys: strain amplitude, frequency and temperature effects. *Journal of Sound and Vibration* 214(5): 885–901.

Popov P and Lagoudas DC (2007) A 3-d constitutive model for shape memory alloys incorporating pseudoelasticity and detwinning of self-accommodated martensite. *International Journal of Plasticity* 23(10-11): 1679–1720.

Saint-Sulpice L, Chirani SA and Calloch S (2009) A 3d superelastic model for shape memory alloys taking into account progressive strain under cyclic loadings. *Mechanics of Materials* 41(1): 12–26.

Tabrizikahou A, Kuczma M, Łasecka-Plura M, et al. (2022) Application and modelling of shape-memory alloys for structural vibration control: state-of-the-art review. *Construction and Building Materials* 342: 127975.

Thiebaud F and Ben Zineb T (2014) Experimental and finite element analysis of superelastic behaviour of shape memory alloy for damping applications. *Mechanics & Industry* 15(5): 371–376.

Tirelli D, Renda V and Bono F (2000) Characterisation of shape memory alloys applications to the retrofitting of brick masonry wall by the pseudo-dynamic method and numerical models. *JRC ISPRA, Internal report*.

Valanis K (1970) A theory of viscoplasticity without a yield surface. part 1. general theory. *Archives of Mechanics* 23: 30.

Xu L, Solomou A, Baxevanis T, et al. (2021) Finite strain constitutive modeling for shape memory alloys considering transformation-induced plasticity and two-way shape memory effect. *International Journal of Solids and Structures* 221: 42–59.

Zhang Z, Bi K, Hao H, et al. (2020) Development of a novel deformation-amplified shape memory alloy-friction damper for mitigating seismic responses of rc frame buildings. *Engineering Structures* 216: 110751.